Supplementary Information

Atomically dispersed nonmagnetic electron traps improve oxygen reduction activity of perovskite oxides

Zechao Zhuang,[a] Yong Li,[b] Yihang Li,[c] Jiazhao Huang,[d] Bin Wei,[e] Rong Sun,[e] Yujing Ren,[f] Jie Ding,[f] Jiexin Zhu,[g] Zhiquan Lang,[h] Lyudmila V. Moskaleva,[b] Chuanxin He,[c] Yu Wang,[i] Zhongchang Wang,[e] Dingsheng Wang*[a] and Yadong Li[a]

[a]Department of Chemistry, Tsinghua University, Beijing, P. R. China

[b]Institute of Applied and Physical Chemistry and Center for Environmental Research and Sustainable Technology, University of Bremen, Bremen, Germany

[c]College of Chemistry and Environmental Engineering, Shenzhen University, Shenzhen, P. R. China

[d]State Key Laboratory of Material Processing and Die & Mould Technology, School of Materials Science and Engineering, Huazhong University of Science and Technology, Wuhan, P. R. China

[e]International Iberian Nanotechnology Laboratory (INL), Braga, Portugal

[f]State Key Laboratory of Catalysis, Dalian National Laboratory for Clean Energy, Dalian Institute of Chemical Physics, Chinese Academy of Sciences, Dalian, P. R. China.

[g]State Key Laboratory of Advanced Technology for Materials Synthesis and Processing, Wuhan University of Technology, Wuhan, P. R. China

[h]Center for Marine Materials Corrosion and Protection, College of Materials, Xiamen University, Xiamen, P. R. China

[i]Shanghai Synchrotron Radiation Facility, Shanghai Institute of Applied Physics, Chinese Academy of Sciences, Shanghai, P. R. China

*E-mail: wangdingsheng@mail.tsinghua.edu.cn

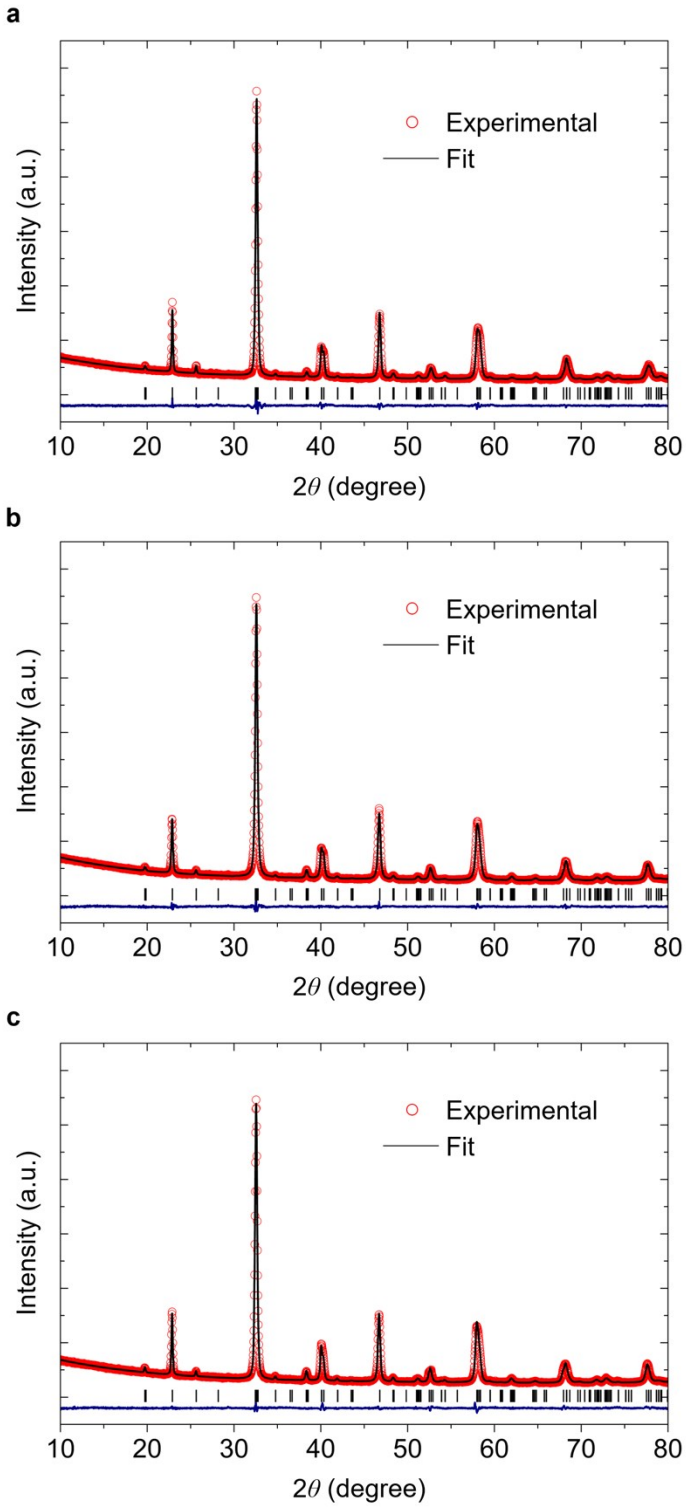

Figure S1. XRD patterns fitted with Rietveld simulation of LCMO (**a**), Mo_1/LCMO-0.02 (**b**), and Mo_1/LCMO-0.06 (**c**).

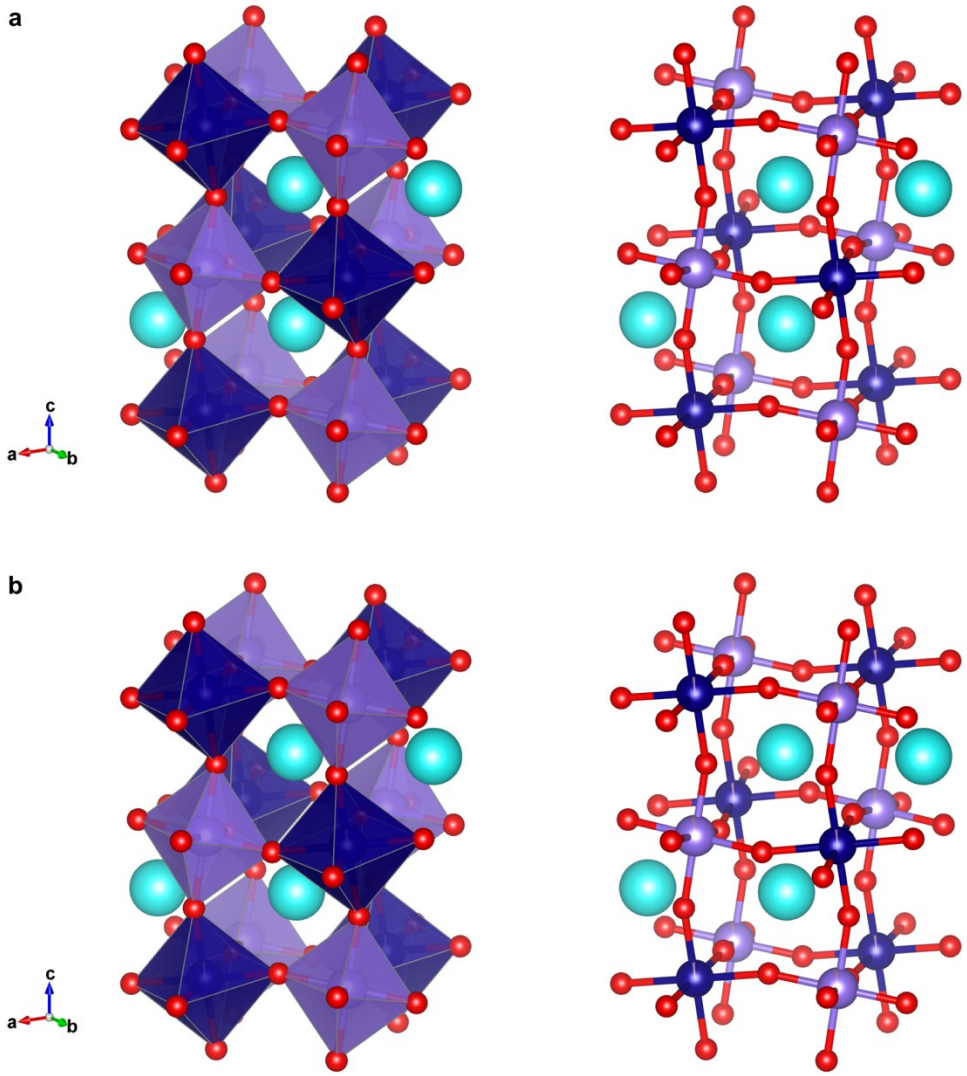

Figure S2. Crystal structures of Mo_1/LCMO-0.02 (**a**) and Mo_1/LCMO-0.06 (**b**).

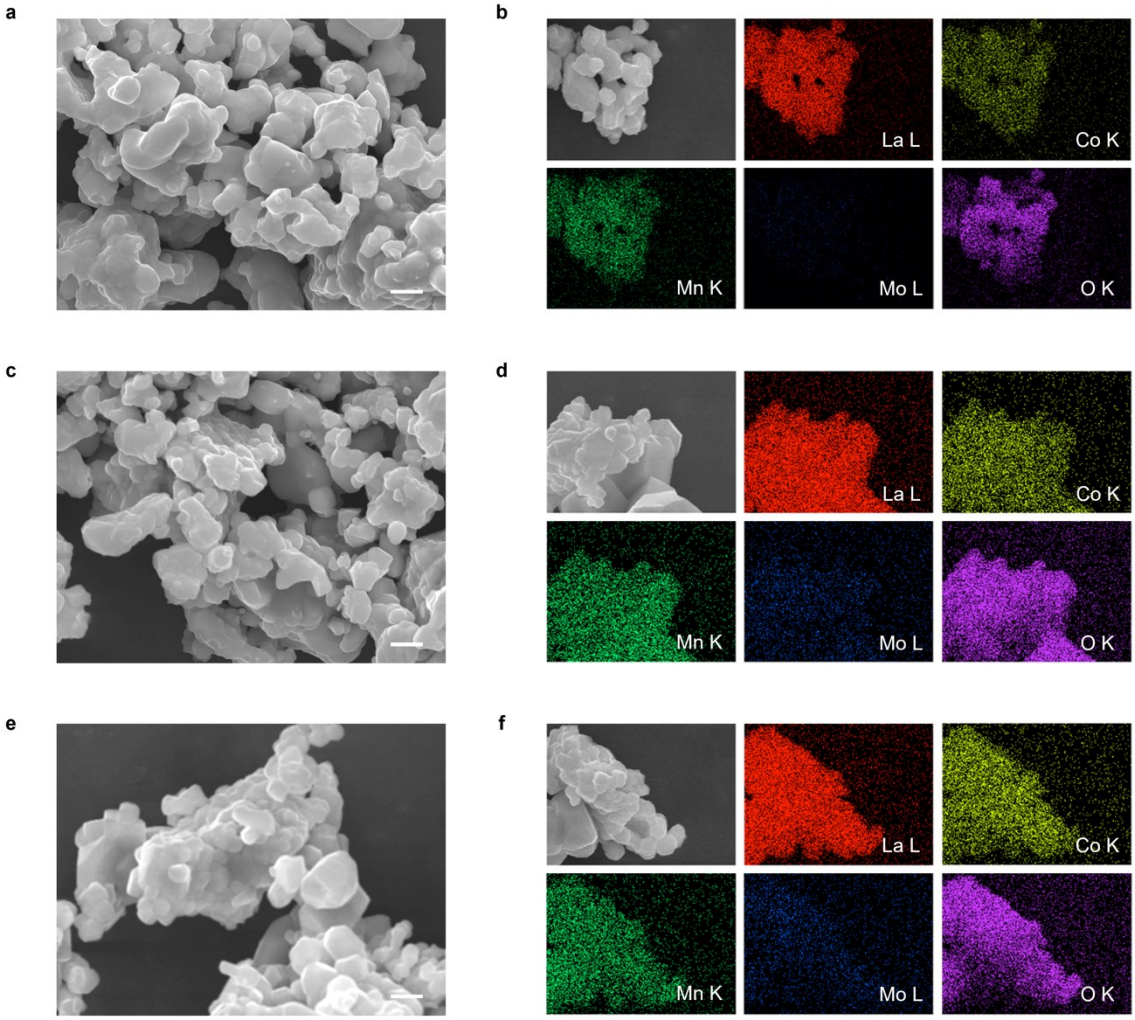

Figure S3. SEM images and EDS mapping of LCMO (**a**, **b**), Mo_1/LCMO-0.02 (**c**, **d**), and Mo_1/LCMO-0.06 (**e**, **f**). Scale bars are 1 μm.

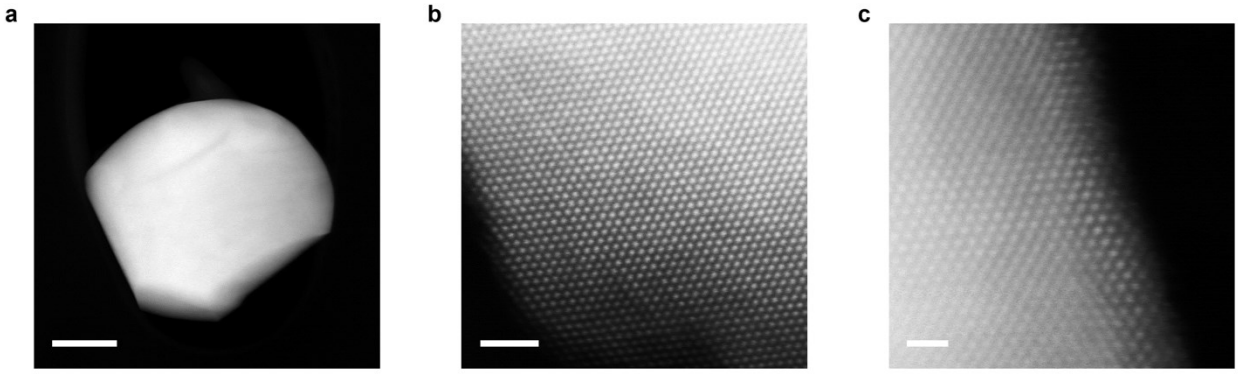

Figure S4. HAADF-STEM images for Mo_1/LCMO-0.06. Scale bars of **a**, **b**, and **c** are 100, 2, and 1 nm, respectively.

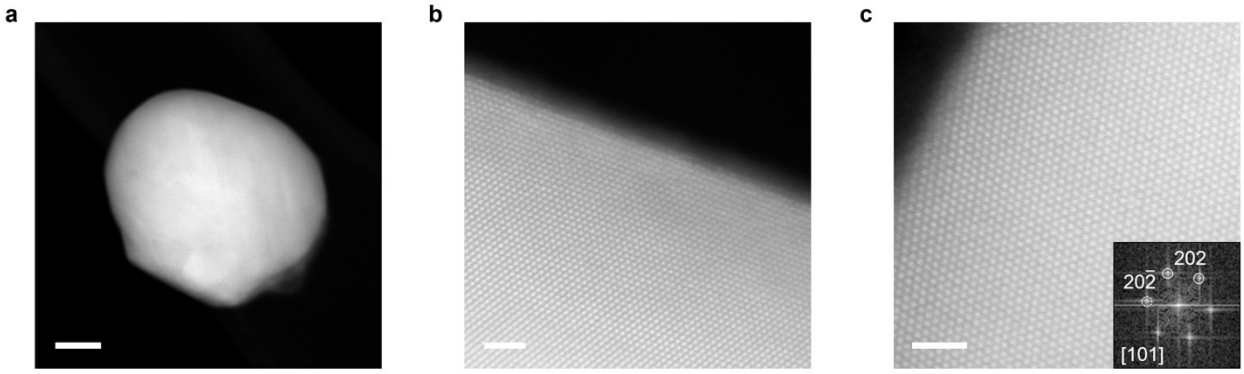

Figure S5. HAADF-STEM images for LCMO. Inset of **c** shows the corresponding fast Fourier transform pattern. Scale bars of **a**, **b**, and **c** are 50, 2, and 2 nm, respectively.

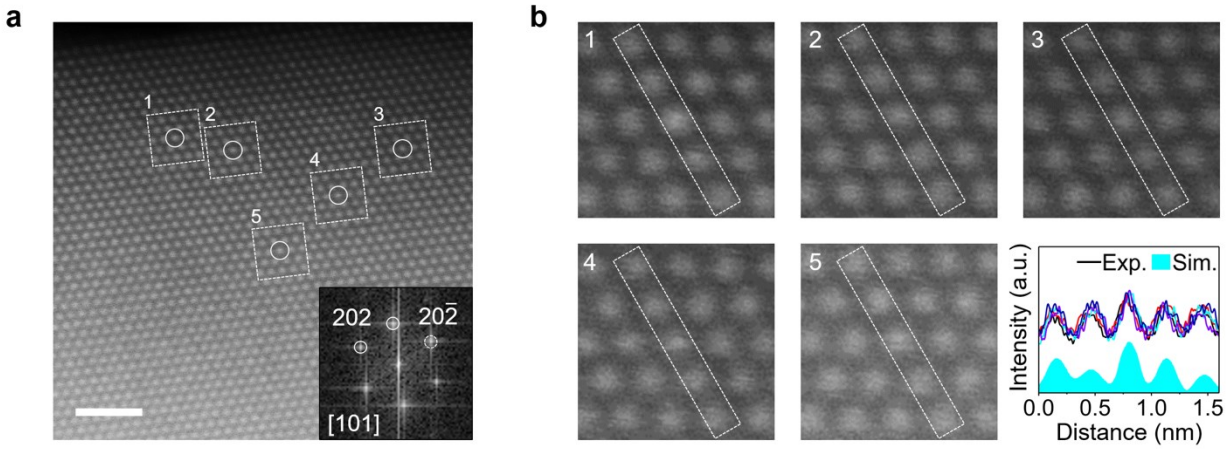

Figure S6. **a**, Atomic-resolution HAADF-STEM image obtained along the [101] zone axis of Mo_1/LCMO. Inset shows the corresponding fast Fourier transform patterns. White circles mark single Mo atoms. Scale bar is 2 nm. **b**, Enlarged view of the regions **1**−**5** marked white in **a** and intensity profile analysis according to the corresponding atomic model of Mo_1/LCMO surface in **Fig. 1(c)**.

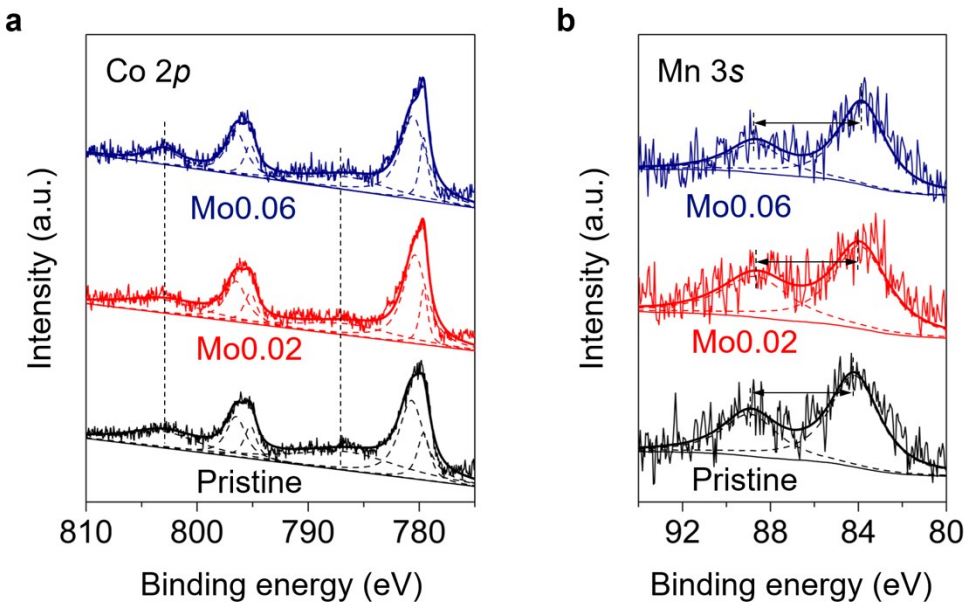

Figure S7. XPS spectra of Co 2*p* (**a**) and Mn 3*s* (**b**) of LCMO and Mo_1/LCMO.

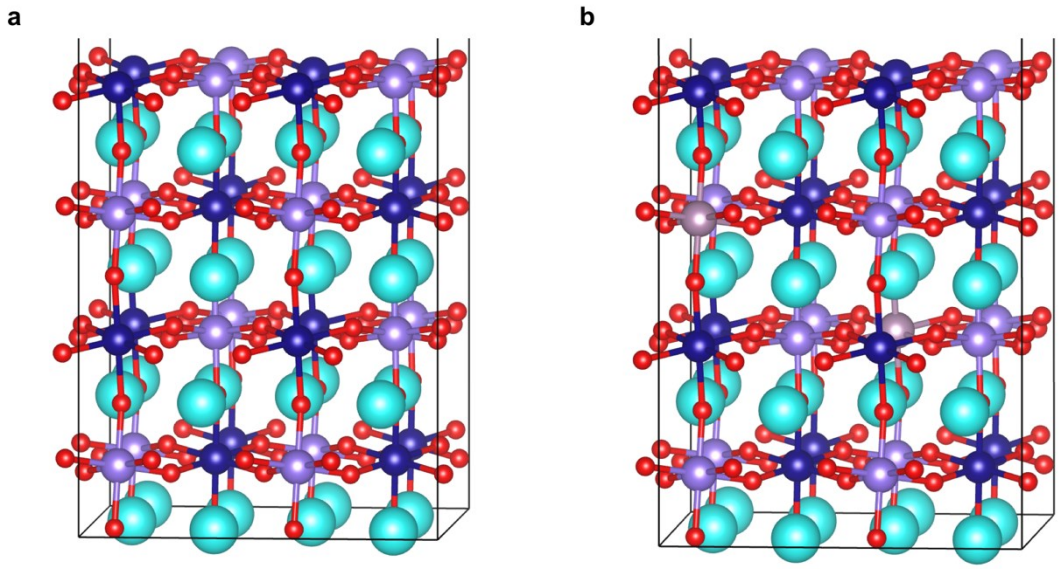

Figure S8. Optimized geometry of bare LCMO (**a**) and Mo_1/LCMO-0.06 (**b**) (001) surface. Gray balls represent Mo atoms.

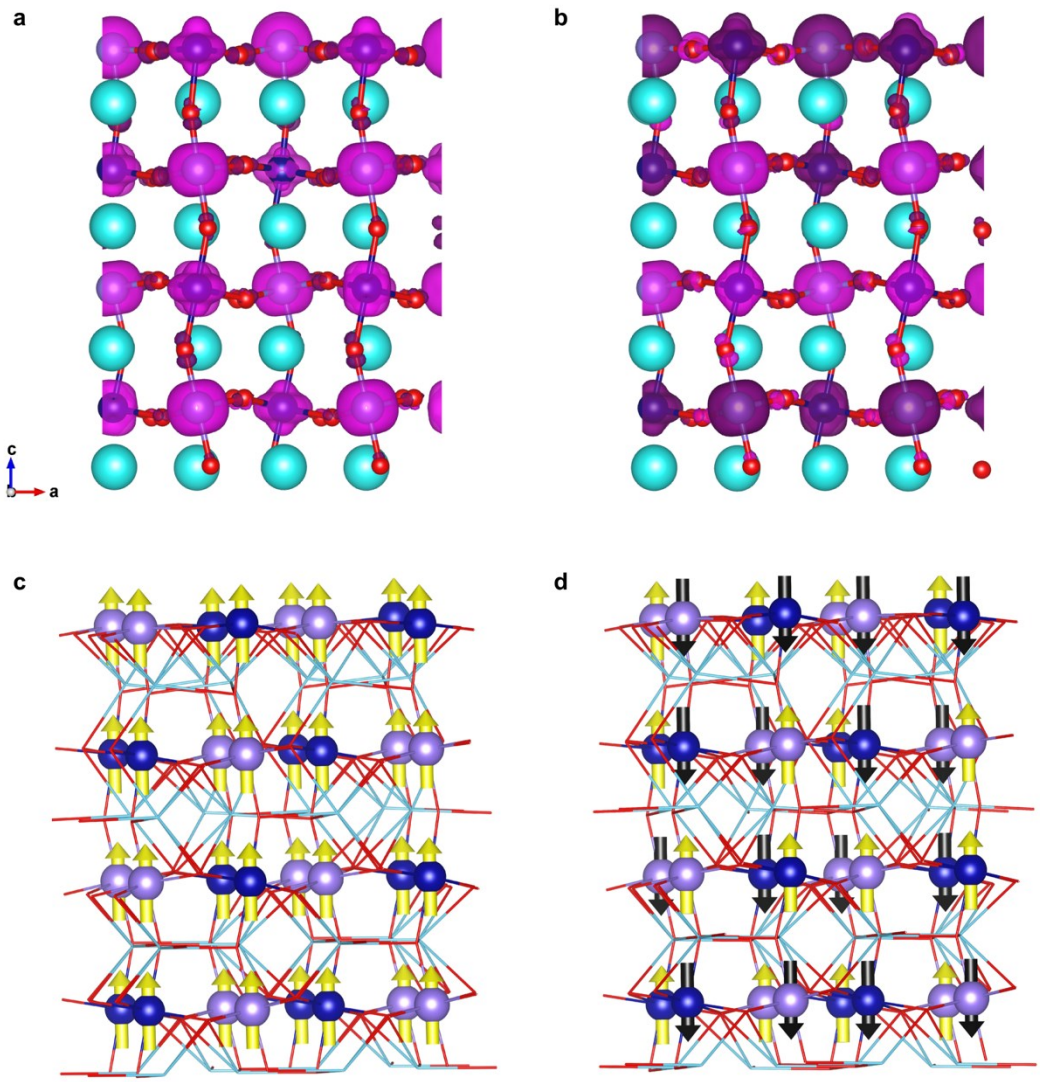

Figure S9. Spin density and spin−spin alignment of ferromagnetic (**a**, **c**) and antiferromagnetic configurations (**b**, **d**) considered for LCMO. Purple and magenta isosurfaces represent alpha and beta spin densities, respectively. Up and down arrows represent alpha spins and beta spins. The ferromagnetic state has a much lower energy than antiferromagnetic one by 1.17 eV.

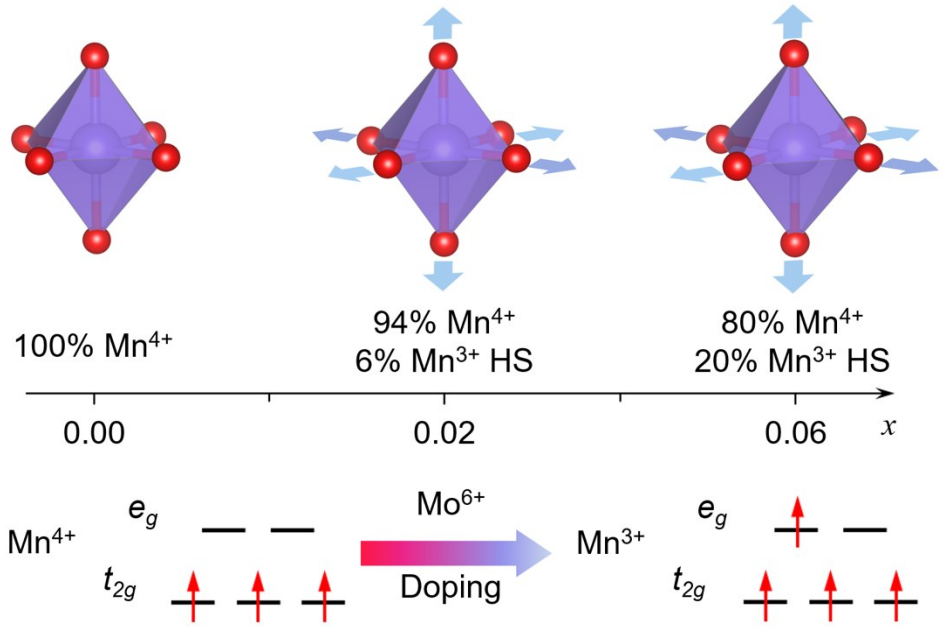

Figure S10. Mo^{6+}-mediated electron trapping at Mn e_g orbitals, inducing valence changes and triaxial MnO_6 octahedra expansion.

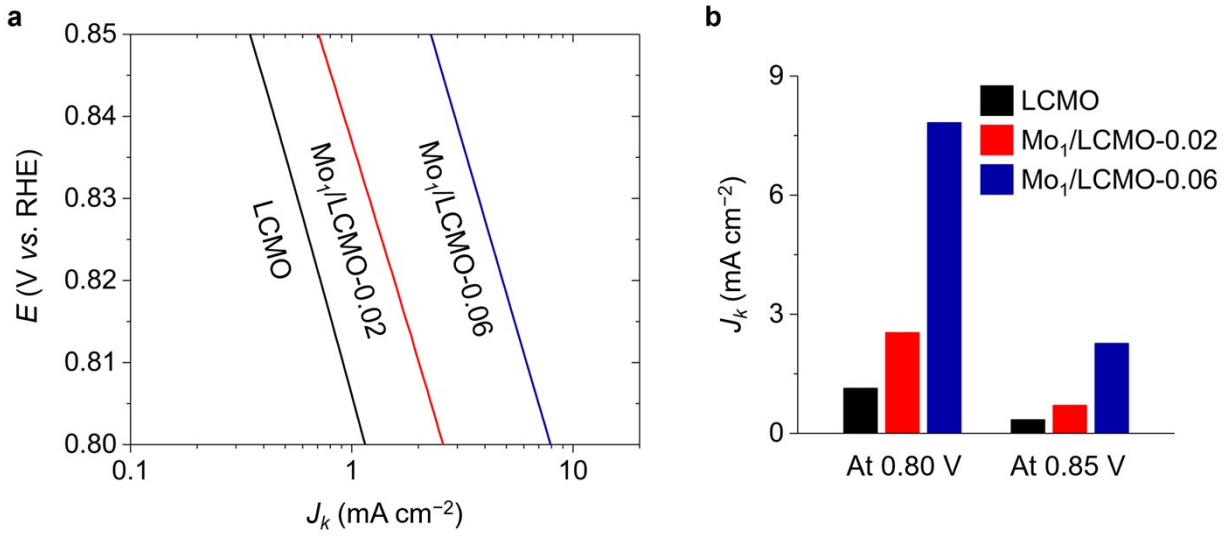

Figure S11. Tafel plots (**a**) and comparison of kinetic current densities at 0.80 and 0.85 V vs. RHE (**b**) of LCMO and Mo_1/LCMO.

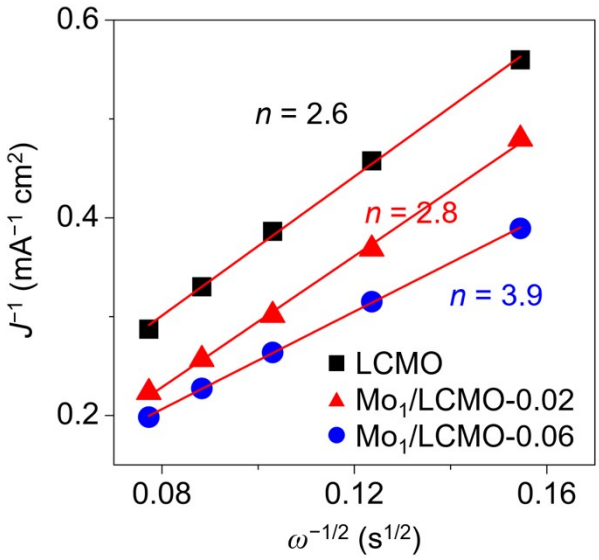

Figure S12. Koutecký−Levich plots of LCMO and Mo_1/LCMO. Compared to the RRDE results in **Fig. 3(d)**, the *n* obtained by Koutecký−Levich plots is very close for Mo_1/LCMO-0.06, namely ~4, but those for LCMO and Mo_1/LCMO-0.02 are slightly smaller. Note that applications of Koutecký−Levich equation have some prerequisites, where the partial order of reaction in respect to oxygen should be equal to one. That of Pt catalysts often exhibits one in alkaline media such that this method is highly applicable to Pt,[1,2] while for oxides, its utility is controversial. Besides, as shown in **Fig. 3(a)**, both LCMO and Mo_1/LCMO-0.02 suffer from the internal diffusion limitations from outermost electrocatalyst layer to electrochemically active sites, therefore the calculation of their *n* values by Koutecký−Levich equation would be affected.[3] Here these results can only be used as reference.

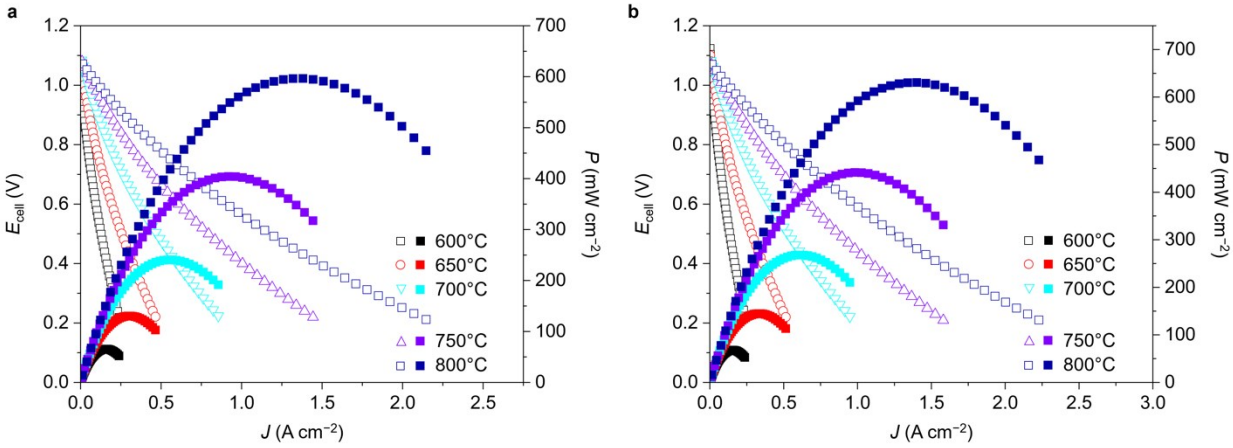

Figure S13. Current−voltage polarization curves and the corresponding power densities of SOFCs with LCMO (**a**) and Mo_1/LCMO-0.02 (**b**) cathodes at 600−800 °C using humidified H_2 as fuel and ambient air as oxidant.

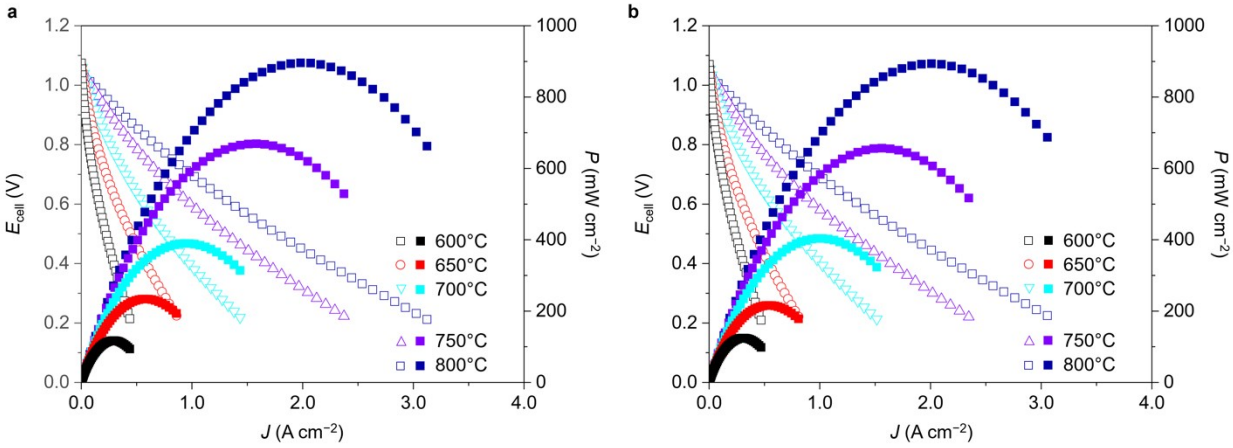

Figure S14. Current−voltage polarization curves and the corresponding power densities of two additional SOFCs with Mo_1/LCMO-0.06 cathode at 600−800 °C using humidified H_2 as fuel and ambient air as oxidant.

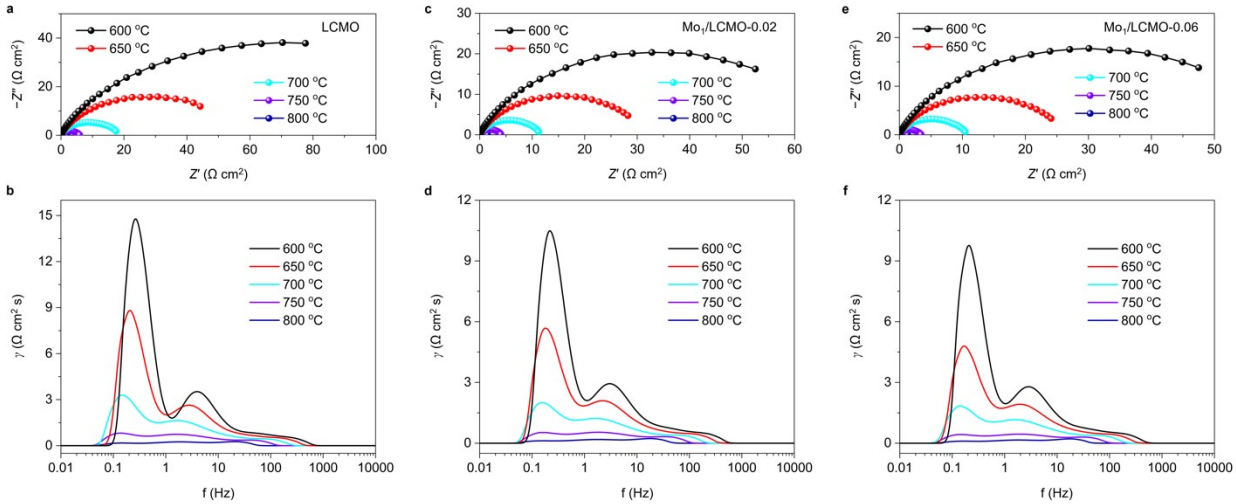

Figure S15. EIS plots (**a**, **c**, **e**) and DRT curves (**b**, **d**, **f**) of symmetric cells at 700 °C.

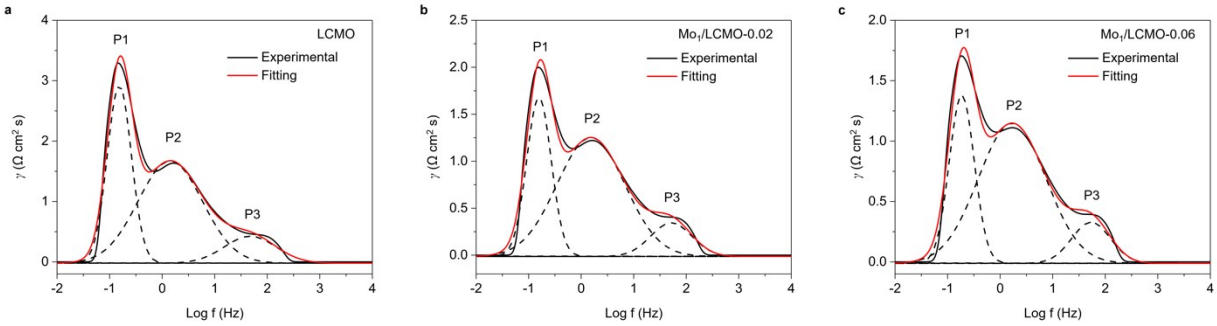

Figure S16. Fits of the DRT curves of symmetric cells at 700 °C. P1, P2, and P3 can be ascribed to the contributions from surface oxygen exchange/oxygen dissociation, electron transport, and oxygen transport, respectively.

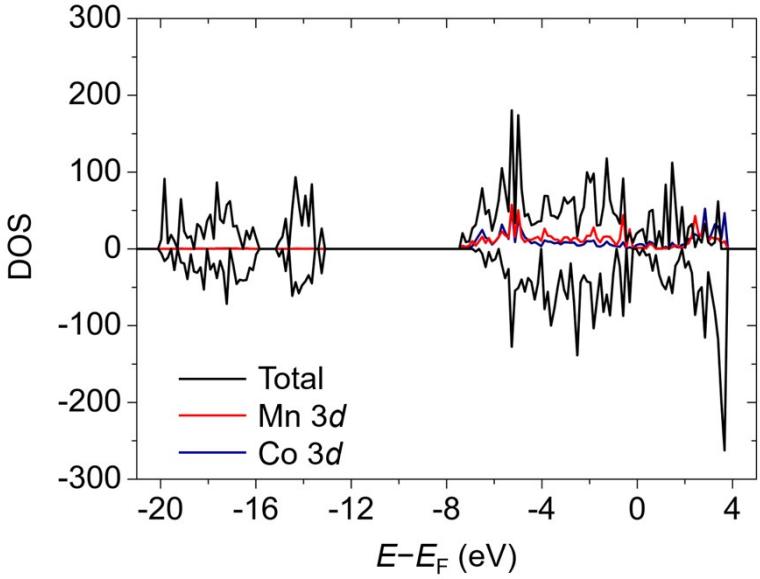

Figure S17. Total DOS, and PDOS onto Mn, and Co 3*d* states for Mo_1/LCMO-0.06. Computed *d*-band centers of Mn and Co 3*d* are at −1.95 and −2.34 eV respectively.

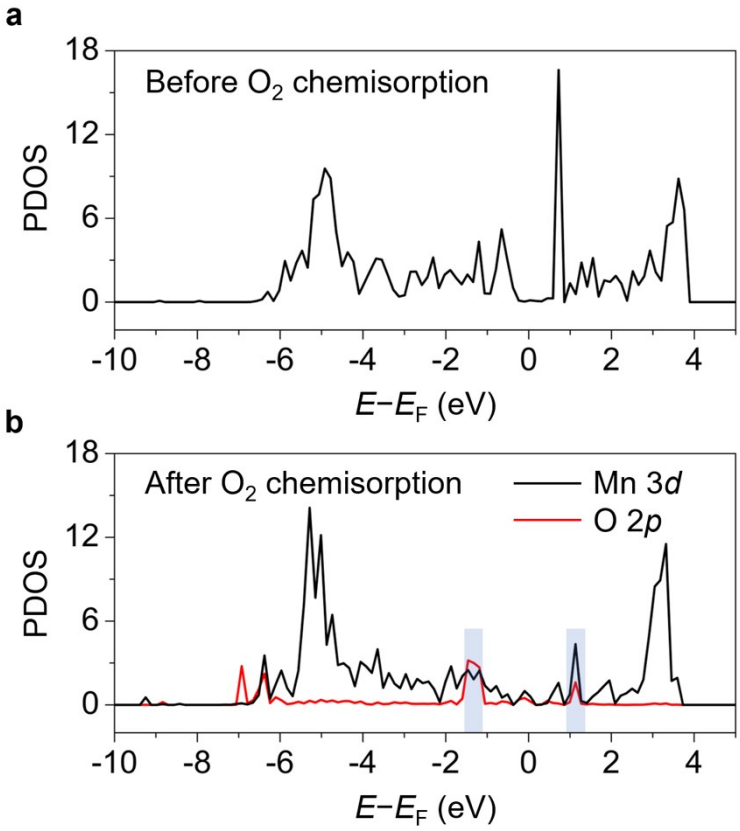

Figure S18. PDOS of O 2*p* and Mn 3*d* states before (**a**) and after O_2 chemisorption (**b**) onto the active surface Mn site.

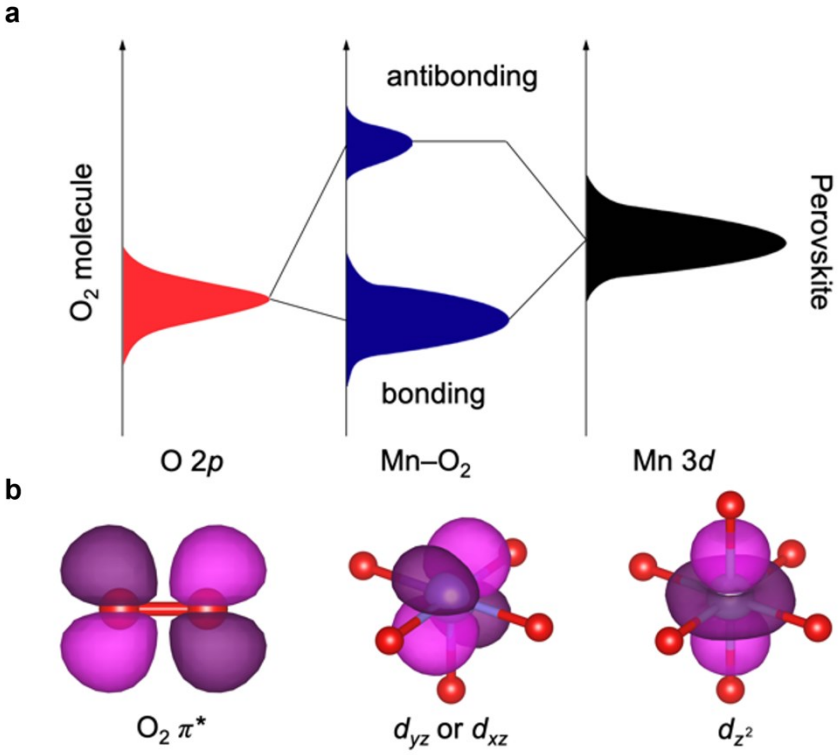

Figure S19. Schematic representation of the orbital interactions (**a**) between O 2$p\pi$* orbital and Mn $3^{d_{xz}}$ or $3^{d_{yz}}$ or $3^{d_{z^2}}$ orbitals (**b**).

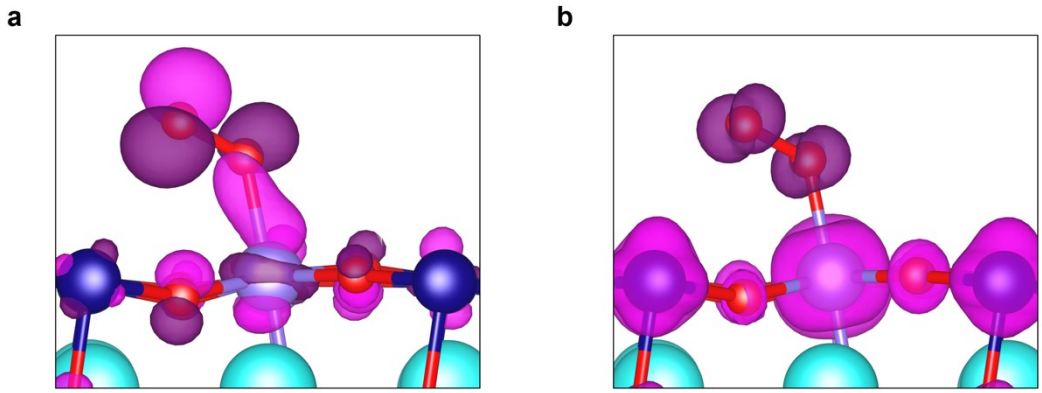

Figure S20. Orbital energy-dependent overlap (**a**) and spatial electron spin density (**b**) of adsorbed O_2 on Mn site with a spin population of 0.96, implying that one electron transfers from Mn to the O_2 molecule.

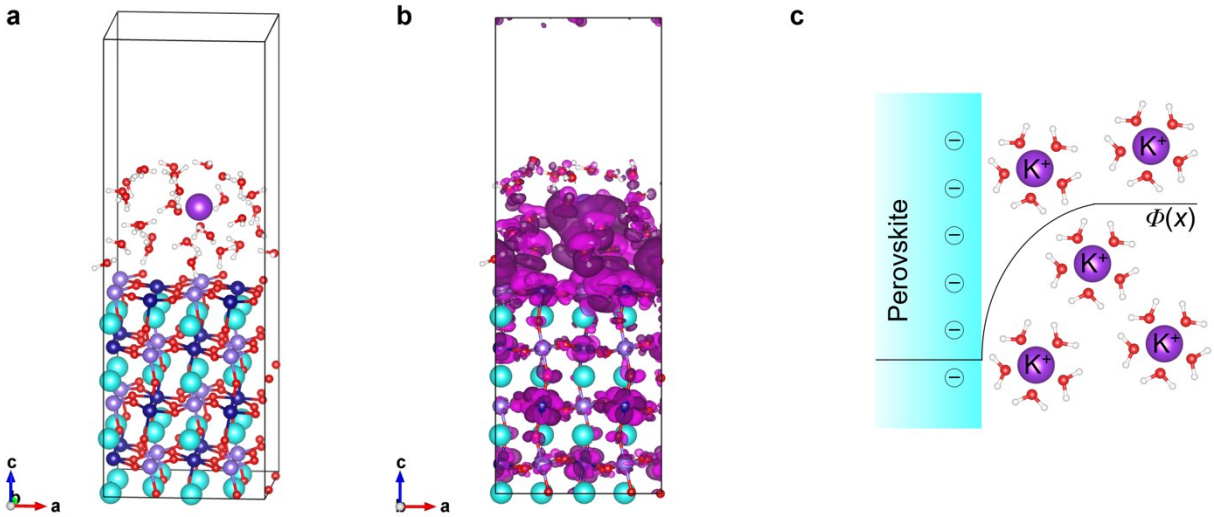

Figure S21. a, Electrical double layer model comprises three layers of water molecules, one positively charged K^+ cation, and a negatively charged perovskite surface. **b**, Charge density difference. Purple and magenta isosurfaces represent negative charges localized mainly on the perovskite surface and positive charges in water layers and K^+. **c**, Schematic representation of the electrical double layer interface.

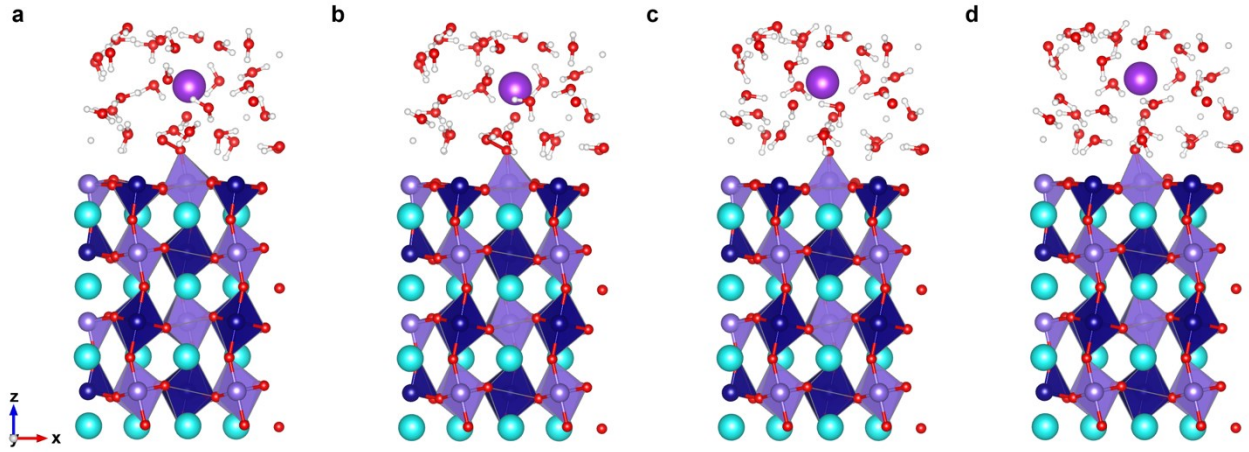

Figure S22. Optimized geometry of perovskite surfaces with adsorbed OO* (**a**), HOO* (**b**), O* (**c**), and HO* intermediates (**d**) , of which the surface at open circuit adsorbs HO*.

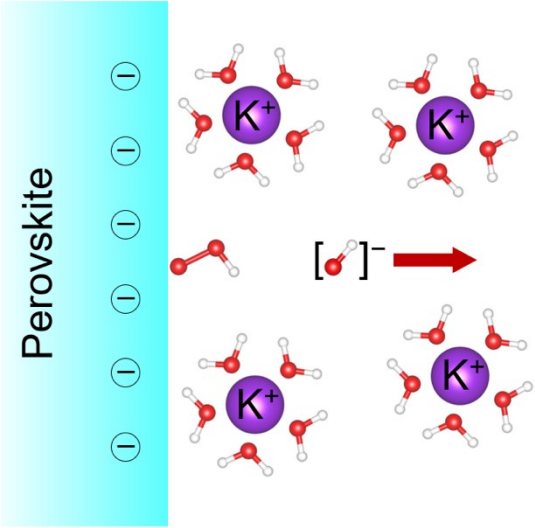

Figure S23. Hydroxyl migration toward anode under an applied electric potential.

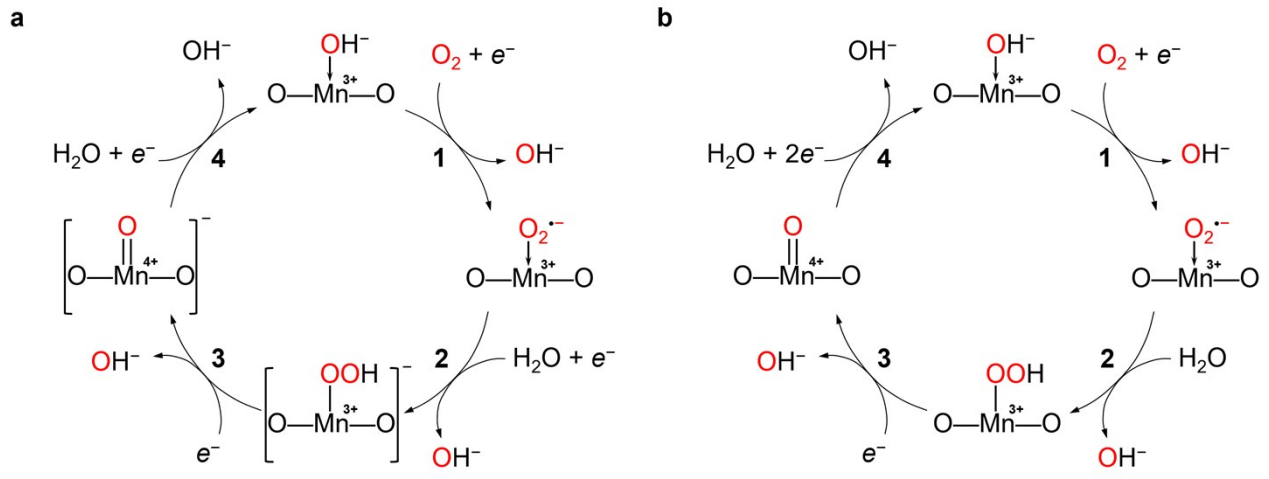

Figure S24. Possible ORR mechanisms on catalytically active Mn^{3+} site. The ORR proceeds via four-electron steps: 1, surface hydroxide displacement; 2, surface peroxide formation; 3, surface oxide formation; 4, surface hydroxide regeneration. Mechanism in (**a**) proceeds via conventional stepwise reduction (four single-electron transfers), forming $[Mn^{3+}–OOH]^{–}$ in **2** and $[Mn^{4+}=O]^{–}$ in **3**. On the considerations of the difficulty in breaking a $Mn^{4+}=O$ double bond, another competitive mechanism in (**b**) is possible via intermittent reduction (two single-electron transfers and one double-electron transfer), where reductive cleavage of $Mn^{4+}=O$ bond requires two electrons and one proton leading to hydroxide regeneration in **4**.

Table S1. Phase identification and structural parameters summary from Rietveld refinement of XRD patterns.

	La_2CoMnO_6	$La_2(CoMn)_{0.99}Mo_{0.02}O_6$	$La_2(CoMn)_{0.97}Mo_{0.06}O_6$
Space group	$P2_1/n$	$P2_1/n$	$P2_1/n$
a /Å	5.5129(1)	5.5140(1)	5.5151(1)
b /Å	5.4620(2)	5.4630(2)	5.4650(1)
c /Å	7.7602(1)	7.7684(2)	7.7724(2)
β /°	90.03(1)	90.03(1)	90.03(1)
La (x, y, z)	0.9894(2), 0.0257(2), 0.2390(1)	0.9895(1), 0.0256(2), 0.2390(4)	0.9892(2), 0.0262(3), 0.2392(1)
Occ., B /Å^2	1, 1.22(2)	1, 1.98(3)	1, 1.93(2)
Co (x, y, z)	0, 0.5, 0	0, 0.5, 0	0, 0.5, 0
Occ., B /Å^2	1, 1.67(1)	0.99, 1.73(2)	0.97, 2.01(1)
Mn (x, y, z)	0.5, 0, 0	0.5, 0, 0	0.5, 0, 0
Occ., B /Å^2	1, 1.03(2)	0.99, 2.52(1)	0.97, 2.91(3)
Mo1 (x, y, z)	-	0, 0.5, 0	0, 0.5, 0
Occ., B /Å^2	-	0.01, 1.08(2)	0.03, 1.86(2)
Mo2 (x, y, z)	-	0.5, 0, 0	0.5, 0, 0
Occ., B /Å^2	-	0.01, 1.59(2)	0.03, 2.04(2)
O1 (x, y, z)	0.0553(2), 0.4934(1), 0.2544(1)	0.0567(1), 0.4964(3), 0.2547(2)	0.0612(2), 0.4997(2), 0.2528(3)
Occ., B /Å^2	1, 2.02(3)	1, 1.39(1)	1, 1.05(2)
O2 (x, y, z)	0.7127(2), 0.2709(3), 0.0219(3)	0.7130(2), 0.2713(1), 0.0262(5)	0.7135(1), 0.2727(3), 0.0327(2)
Occ., B /Å^2	1, 3.78(2)	1, 1.78(1)	1, 4.96(4)
O3 (x, y, z)	0.7442(2), 0.2857(2), 0.4660(2)	0.7440(1), 0.2849(3), 0.4626(4)	0.7439(2), 0.2839(1), 0.4593(3)
Occ., B /Å^2	1, 1.45(2)	1, 1.35(1)	1, 1.11(2)
R_{wp}	2.12	2.40	2.29
χ^2	1.38	1.42	1.54

Table S2. Co−O and Mn−O bond distances from structure analysis results in Table S1 (Å).

	La_2CoMnO_6	$La_2(CoMn)_{0.99}Mo_{0.02}O_6$	$La_2(CoMn)_{0.97}Mo_{0.06}O_6$
Co−O1	1.9977(2)	2.0028(3)	1.9938(2)
Co−O2	2.0258(1)	2.0267(2)	2.0261(1)
Co−O3	2.0778(1)	2.0778(1)	2.0776(2)
Mn−O1	1.9307(3)	1.9317(2)	1.9507(1)
Mn−O2	1.8955(2)	1.9018(1)	1.9161(2)
Mn−O3	1.8516(1)	1.8595(2)	1.8681(2)

Table S3. Co−O and Mn−O angles from structure analysis results in Table S1 (°).

	La_2CoMnO_6	$La_2(CoMn)_{0.99}Mo_{0.02}O_6$	$La_2(CoMn)_{0.97}Mo_{0.06}O_6$
Co−O1−Mn	162.02	161.66	160.28
Co−O2−Mn	163.39	162.15	159.95
Co−O3−Mn	161.82	160.57	159.37

Table S4. Brunauer−Emmett−Teller (BET) surface areas of perovskite oxides.

	BET surface area (m^2 g^{-1})
La_2CoMnO_6	1.30
$La_2(CoMn)_{0.99}Mo_{0.02}O_6$	1.35
$La_2(CoMn)_{0.97}Mo_{0.06}O_6$	1.25

Table S5. Comparison of intrinsic ORR activities for different oxide catalysts according to the evaluation method proposed by Suntivich *et al*.[4]

Catalysts	Potential (V vs. RHE) @25 μA cm_{ox}^{-2}	References
Mo_1/LCMO	**0.99**	**This wotk**
$LaMnO_{3+\delta}$	0.92	*Nat. Chem.* **2011**, *3*, 546
$LaNiO_3$	0.92	*Nat. Chem.* **2011**, *3*, 546
$La_{0.5}Ca_{0.5}MnO_3$	0.89	*Nat. Chem.* **2011**, *3*, 546
$MnCo_2O_4$	0.89	*Adv. Mater.* **2017**, *29,* 1606800
$LaCoO_3$	0.86	*Nat. Chem.* **2011**, *3*, 546
$Mn_{2.5}Co_{0.5}O_4$	0.84	*Adv. Mater.* **2017**, *29,* 1606800
Mn_2CoO_4	0.84	*Adv. Mater.* **2017**, *29,* 1606800
$LaMnO_3$	0.85	*Nat. Chem.* **2011**, *3*, 546
$LaMn_{0.5}Ni_{0.5}O_3$	0.82	*Nat. Chem.* **2011**, *3*, 546
$LaMn_{0.5}Cu_{0.5}O_3$	0.80	*Nat. Chem.* **2011**, *3*, 546
$La_4Ni_3O_7$	0.80	*Nat. Chem.* **2011**, *3*, 546
$NiCo_2O_4$	0.80	*Adv. Mater.* **2017**, *29,* 1606800
Mn_3O_4	0.79	*Adv. Mater.* **2017**, *29,* 1606800
$LiMn_2O_4$	0.78	*Adv. Mater.* **2017**, *29,* 1606800
$Li_{0.74}Mn_2O_4$	0.76	*Adv. Mater.* **2017**, *29,* 1606800
$La_{0.5}Ca_{0.5}CoO_{3-\delta}$	0.75	*Nat. Chem.* **2011**, *3*, 546
$MnFe_2O_4$	0.75	*Adv. Mater.* **2017**, *29,* 1606800
$ZnCo_2O_4$	0.74	*Adv. Mater.* **2017**, *29,* 1606800
La_2NiO_4	0.73	*Nat. Chem.* **2011**, *3*, 546
Co_3O_4	0.73	*Adv. Mater.* **2017**, *29,* 1606800
$La_{0.5}Ca_{0.5}FeO_3$	0.71	*Nat. Chem.* **2011**, *3*, 546
$La_{0.75}Ca_{0.25}FeO_3$	0.70	*Nat. Chem.* **2011**, *3*, 546
$CoFe_2O_4$	0.70	*Adv. Mater.* **2017**, *29,* 1606800
$NiFe_2O_4$	0.70	*Adv. Mater.* **2017**, *29,* 1606800
$LaCrO_3$	0.69	*Nat. Chem.* **2011**, *3*, 546

Table S6. Electrical resistivity for perovskite oxides at room temperature.

	Resistivity ($\mu\Omega$ cm)
$CaMnO_3$	6.3×10^3
$CaMn_{0.95}Mo_{0.05}O_3$	4.8×10^1
$SrMnO_3$	1.1×10^4
$SrMn_{0.95}Mo_{0.05}O_3$	1.9×10^2
$LaNiO_3$	2.4×10^1
$LaNi_{0.95}Mo_{0.05}O_3$	1.8
La_2NiMnO_6	2.1×10^7
$La_2(NiMn)_{0.97}Mo_{0.06}O_6$	5.7×10^5

Table S7. Comparison of SOFC performance (@800 °C, mW cm^{-2}) between our cathode catalysts and the state-of-the-art catalysts reported in literatures.

Cathode catalysts	Electrolyte||Anode	Test conditions	Power density	References
Mo_1/LCMO	**GDC||YSZ||Ni-YSZ**	**80 mL min^{-1} H_2; ambient air**	**880**	**This wotk**
$Nd_{0.5}Sr_{0.5}CoO_3$	GDC||YSZ||Ni-YSZ	80 mL min^{-1} H_2; ambient air	800	*Energy and AI* 2020, *2*, 100027
$Sr_2Fe_{1.5}Mo_{0.5}O_6$	LSGM||GDC||Ni-GDC	80 mL min^{-1} H_2; ambient air	418	*J. Mater. Chem. A* 2020, *8*, 14091
$La_{1.7}Bi_{0.2}Sr_{0.1}CuO_4$	SDC||YSZ||Ni-YSZ	50 mL min^{-1} H_2; ambient air	630	*ACS Appl. Mater. Interface* 2019, *11*, 21593
$LaSrCoTiO_5$	LSGM||SDC||Ni-SDC	100 mL min^{-1} H_2; ambient air	776	*Int. J. Hydrogen Energy* 2016, *41*, 21439
Nd_2NiO_4	YSZ||Ni-YSZ	100 mL min^{-1} H_2; 100 mL min^{-1} 20%O_2+80%N_2	1300	*J. Mater. Chem. A* 2014, *2*, 9764
$La_{0.6}Sr_{0.4}Co_{0.2}Fe_{0.8}O_3$	GDC||YSZ||Ni-YSZ	80 mL min^{-1} H_2; ambient air	401	*J. Power Sources* 2014, *268*, 634
$La_{0.6}Sr_{0.4}Co_{0.2}Fe_{0.8}O_3$	GDC||YSZ||Ni-YSZ	80 mL min^{-1} H_2; ambient air	695	*Ceram. Int.* 2015, *41*, 7651
$La_{0.6}Sr_{0.4}Co_{0.2}Fe_{0.8}O_3$	GDC||YSZ||Ni-YSZ	H_2; unknown	780	*Appl. Catalysis B: Environ. 2020, 268,* 118413
$La_{0.6}Sr_{0.4}Co_{0.2}Fe_{0.8}O_3$	GDC||YSZ||Ni-YSZ	200 mL min^{-1} H_2; 200 mL min^{-1} air	1220	*Energy Environ. Sci. 2012, 5,* 7066
$La_{0.6}Sr_{0.4}FeO_3$	YSZ||Ni-YSZ	50 mL min^{-1} H_2; 50 mL min^{-1} air	506	*Appl. Energy 2019, 241,* 1
$NdBa_{0.5}Ca_{0.5}Co_{1.5}Fe_{0.5}O_5$	GDC||YSZ||Ni-YSZ	100 mL min^{-1} H_2; ambient air	941	*J. Energy Chem.* 2020, *43*, 108
$La_{0.8}Sr_{0.2}MnO_3$	YSZ||Ni-YSZ	100 mL min^{-1} H_2; ambient air	470	*J Mater Chem A 2018, 6,* 2721
$La_{0.8}Sr_{0.2}MnO_3$	YSZ||Ni-YSZ	30 mL min^{-1} H_2; ambient air	580	*Nat. Commun.* 2019, *10*, 1497.
$La_{0.8}Sr_{0.2}MnO_3$	YSZ||Ni-YSZ	30 mL min^{-1} H_2; 50 mL min^{-1} air	980	*Energy Environ. Sci. 2018, 11,* 2390
$(La_{0.8}Sr_{0.2})_{0.95}MnO_3$	YSZ||Ni-YSZ	30 mL min^{-1} H_2; ambient air	780	*J. Power Sources 2015, 274,* 1114

Table S8. Fitting results of the DRT curves of symmetric cells composed of LCMO cathodes and YSZ electrolyte at 700 °C.

Cathode	ASR (Ω cm^2)	Peak1	R1 (Ω cm^2)	Peak2	R2 (Ω cm^2)	Peak3	R3 (Ω cm^2)
LCMO	17.49	0.1132	1.97988	0.53583	9.37159	0.35097	6.13853
$La_2(CoMn)_{0.99}Mo_{0.02}O_6$	11.23	0.10334	1.16053	0.6042	6.78521	0.29245	3.28426
$La_2(CoMn)_{0.97}Mo_{0.06}O_6$	9.60	0.10394	0.99781	0.62004	5.95238	0.27602	2.64981

Reference

1 A. Damjanovic, A. Dey and J. O. Bockris, *Electrochim. Acta*, 1966, **11**, 791.

2 A. R. Zeradjanin, *ChemSusChem*, 2018, **11**, 1278.

3 S. T. Dix, S. Lu and S. Linic, *ACS Catal.*, 2020, **10**, 10735.

4 J. Suntivich, H. A. Gasteiger, N. Yabuuchi, H. Nakanishi, J. B. Goodenough and Y. Shao-Horn, *Nat. Chem.*, 2011, **3**, 546−550.